The Stirring Tropics: The Ubiquity of Moisture Modes and Moisture–Vortex Instability

VÍCTOR C. MAYTA[a] AND ÁNGEL F. ADAMES CORRALIZA[a]

[a] *Department of Atmospheric and Oceanic Sciences, University of Wisconsin–Madison, Madison, Wisconsin*

(Manuscript received 14 March 2023, in final form 8 December 2023, accepted 10 January 2024)

ABSTRACT: Observations of column water vapor in the tropics show significant variations in space and time, indicating that it is strongly influenced by the passage of weather systems. It is hypothesized that many of the influencing systems are moisture modes, systems whose thermodynamics are governed by moisture. On the basis of four objective criteria, results suggest that all oceanic convectively coupled tropical depression (TD)-like waves and equatorial Rossby waves are moisture modes. These modes occur where the horizontal column moisture gradient is steep and not where the column water vapor content is high. Despite geographical basic-state differences, the moisture modes are driven by the same mechanisms across all basins. The moist static energy (MSE) anomalies propagate westward by horizontal moisture advection by the trade winds. Their growth is determined by the advection of background moisture by the anomalous meridional winds and anomalous radiative heating. Horizontal maps of column moisture and 850-hPa streamfunction show that convection is partially collocated with the low-level circulation in nearly all the waves. Both this structure and the process of growth indicate that the moisture modes grow from moisture–vortex instability. Last, space–time spectral analysis reveals that column moisture and low-level meridional winds are coherent and exhibit a phasing that is consistent with a poleward latent energy transport. Collectively, these results indicate that moisture modes are ubiquitous across the tropics. That they occur in regions of steep horizontal moisture gradients and grow from moisture–vortex instability suggests that these gradients are inherently unstable and are subject to continuous stirring.

SIGNIFICANCE STATEMENT: Over the tropics, column water vapor has been found to be highly correlated with precipitation, especially in slowly evolving systems. These observations and theory support the hypothesis that moisture modes exist, a type of precipitating weather system that does not exist in dry theory. In this study, we found that all oceanic tropical depression (TD)-like waves and equatorial Rossby waves are moisture modes. These systems exist in regions where moisture varies greatly in space, and they grow by transporting air from the humid areas of the tropics toward their low pressure center. These results indicate that the climatological-mean distribution of moisture in the tropics is unstable and is subject to stirring by moisture modes.

KEYWORDS: Convection; Energy transport; Atmospheric waves

1. Introduction

The tropical belt (~25°S–25°N) is characterized by weak spatial and temporal variability of temperature (e.g., Charney 1963; Sobel and Bretherton 2000; Sobel et al. 2001). In contrast, the tropics show a large variability of column water vapor (Fig. 1) that strongly influences the distribution of precipitation (Bretherton et al. 2004). These features lead to one important consequence: the existence of the so-called moisture modes. Moisture modes can be defined as a type of tropical motion where water vapor plays a central role in its dynamics. The term "moisture modes" was initially introduced in Yu and Neelin (1994) to refer to a kind of wave characterized by a large humidity signal. The early conception of moisture modes by Sobel et al. (2001) revealed these systems to be akin to Rossby waves that propagate due to the horizontal advection of the background moisture gradient by the anomalous winds. Since the core dynamics of moisture modes lie in the interaction between moisture and convection, they are a type of tropical motion that is distinct from the dry equatorial waves of Matsuno (1966).

Denotes content that is immediately available upon publication as open access.

Supplemental information related to this paper is available at the Journals Online website: https://doi.org/10.1175/JCLI-D-23-0145.s1.

Corresponding author: Víctor C. Mayta, mayta@wisc.edu

DOI: 10.1175/JCLI-D-23-0145.1

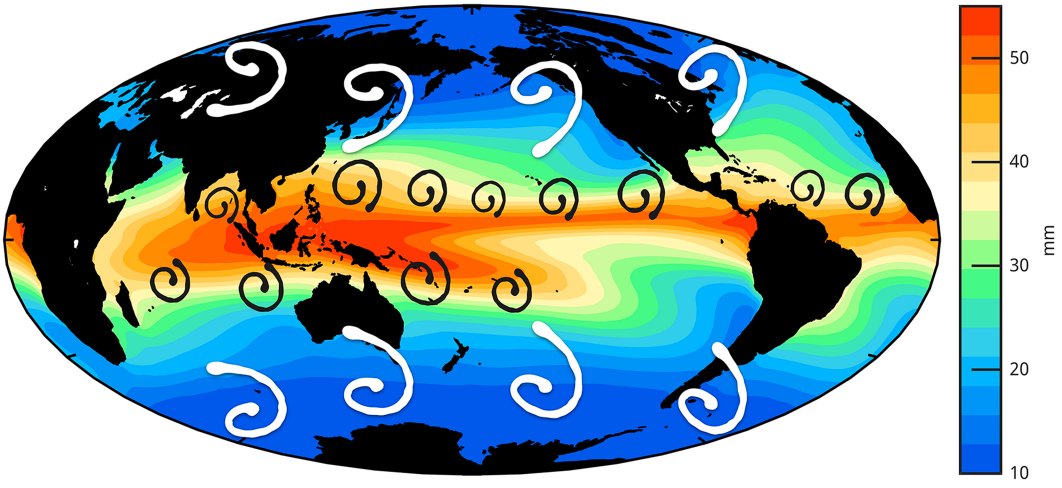

FIG. 1. Annual mean distribution of column-integrated water vapor ($\langle q \rangle$). The black whirls denote tropical eddies that stir $\langle q \rangle$ in the tropics, behaving as a tropical analog to midlatitude eddies (white whirls).

With its distinct space–time spectral signature, the Madden–Julian oscillation (Madden and Julian 1972) was the first tropical phenomenon hypothesized to be a moisture mode (e.g., Raymond and Fuchs 2009; Sobel and Maloney 2012; Adames and Kim 2016; Zhang et al. 2020). The majority of applications of the so-called "moisture mode theory" have since focused on the MJO. More recent studies have suggested that other tropical motions can be moisture modes as well (Gonzalez and Jiang 2019; Adames et al. 2019; Inoue et al. 2020). More recently, Adames (2022) suggested that two types of moisture modes exist: (i) equatorial moisture modes such as the MJO (Raymond et al. 2009; Adames and Kim 2016; Jiang et al. 2018; Zhang et al. 2020) and equatorial Rossby waves (Gonzalez and Jiang 2019; Inoue et al. 2020; Mayta et al. 2022) and (ii) off-equatorial moisture modes such as Pacific easterly waves and monsoon low pressure systems (Serra et al. 2008; Rydbeck and Maloney 2015; Diaz and Boos 2021).

However, what constitutes a moisture mode? Ahmed et al. (2021) and Mayta et al. (2022) proposed three criteria to identify moisture modes: their moisture anomalies must dominate the distribution of moist static energy (MSE) and are in phase with the precipitation anomalies, and the thermodynamic equation must be in weak temperature gradient (WTG) balance. By using the aforementioned criteria, Mayta et al. (2022) found that moisture modes exist outside the warm pool region. They documented that the slowly propagating equatorial Rossby wave over the Western Hemisphere satisfies all conditions to be considered a moisture mode, in agreement with the scale analysis of Adames (2022). More recently, Mayta and Adames (2023) documented the existence of the second moisture mode over the Western Hemisphere, TD-like waves. Vargas-Martes et al. (2023) found that east Pacific easterly waves also satisfy all the criteria to be referred to as moisture modes, while African easterly waves (AEWs) do not. A case study of a developing AEW by Núñez Ocasio and Rios-Berrios (2023) also found that they did not satisfy the criteria to be called moisture modes. Thus, it appears that only oceanic TD-like waves behave like moisture modes. The structural features of the Western Hemisphere equatorial Rossby wave are akin to an equatorial moisture mode, while the features of Atlantic TD-like waves are akin to off-equatorial moisture modes.

While the Western Hemisphere equatorial Rossby wave shares many of the features of its dry shallow water counterpart (Matsuno 1966), the processes responsible for its propagation and growth are different. Rather than propagating westward through the beta effect, the trade winds are responsible for the westward propagation of the Western Hemisphere equatorial Rossby wave. Advection of background-mean MSE by the anomalous meridional winds contributes to its growth (Mayta et al. 2022). This type of growth was initially documented in the balanced moisture waves of Sobel et al. (2001) and was later referred to as moisture–vortex instability (MVI; Adames and Ming 2018a; Adames 2021) or the rotational stratiform instability by Russell et al. (2020). Similar results were found by Gonzalez and Jiang (2019) for western Pacific equatorial Rossby waves. Thus, these equatorial Rossby waves behave in a manner that is more consistent with moisture mode theory, and not following dry shallow water theory with a reduced equivalent depth, as discussed by Mayta et al. (2022). Similar results were also found by Ahmed et al. (2021) and Ahmed (2021).

Given that slowly propagating waves exist throughout the tropics, and that MVI only requires a meridional MSE gradient and coupling between moisture and precipitation, we hypothesize that most observed oceanic TD-like waves and equatorial Rossby waves are moisture modes (Fig. 1). This possibility leads to the main questions of this study:

1) Q1: Are moisture modes common throughout the tropics?
2) Q2: If so, where are they most common?
3) Q3: Is moisture–vortex instability the main destabilization mechanism of moisture modes worldwide?

The paper is organized as follows. Section 2 provides a description of the datasets and analysis methods. A brief

TABLE 1. Region chosen for the thermodynamic analyzes associated with the TD-like and equatorial Rossby waves. To investigate TD-like waves and equatorial Rossby waves, EOFs are calculated over the region of maximum variance across the tropics (Fig. 3). The variance explained by the two leading patterns (PC1 and PC2) is also shown in the last two columns.

Wave	Region	Base point/domain	PC1	PC2
TD-like	Atlantic (AT)	0°–20°N, 70°–10°W	10.9%	10.6%
	Eastern Pacific (EP)	0°–20°N, 130°–80°W	12.8%	12.7%
	Western Pacific (WP)	0°–20°N, 110°E–180°	11.1%	11.0%
	Indian Ocean (IO)	0°–20°N, 70°–100°E	19.4%	18.1%
Equatorial Rossby	Atlantic (AT)	5°S–25°N, 125°W–0°	13.4%	12.8%
	Western Pacific (WP)	25°S–25°N, 110°E–150°W	14.7%	11.6%
	Indian Ocean (IO)	20°S–25°N, 50°–110°E	7.9%	6.9%

introduction of MVI is offered in section 3. In section 4, we elucidate the horizontal structure of TD-like and equatorial Rossby waves and their associated convection on the basis of a linear regression analysis. Section 5 examines the governing thermodynamics for all disturbances. In section 6, we investigate vortex stretching in moisture waves. Section 7 involves a thorough analysis of the MSE budget for each wave type. The assessment of poleward eddy moisture fluxes is presented in section 8. Finally, a summary and discussion are given in section 9.

2. Data and methods

a. *Satellite CLAUS brightness temperature and reanalysis dataset*

Satellite-observed brightness temperature (T_b) has long served as a proxy for tropical convection and we used it in this study. The data are obtained from the Cloud Archive User System (CLAUS) satellite data (Hodges et al. 2000), which has eight-times-daily global fields of T_b from July 1983 to June 2009 and extended through 2017 using the merged IR dataset from NOAA. For dynamical and thermodynamical characteristics associated with TD-like and equatorial Rossby waves, atmospheric variables from the fifth reanalysis of the European Centre for Medium-Range Weather Forecasts (ECMWF) (ERA5; Hersbach et al. 2019) data are used. The temporal resolution is 6 h, the spatial resolution is 0.5° × 0.5° in longitude and latitude, and there are 27 layers ranging from 1000 to 100 hPa for the 36-yr period 1984–2015.

b. *Wave-type filtering, EOF calculation, and regressions*

This work uses filters based on spatiotemporal Fourier decomposition documented in Wheeler and Kiladis (1999) and uses the same frequency–wavenumber domain described in previous studies (e.g., Kiladis et al. 2009; Feng et al. 2020). This is achieved in the wavenumber–frequency domain by retaining only those spectral coefficients within a specific range corresponding to the spectral peaks associated with TD-like and equatorial Rossby waves. T_b is filtered using a fast Fourier transform retaining wavenumbers $k = -20$ to 0 and periods between 10 and 96 days for equatorial Rossby waves as in Mayta et al. (2022). For TD-like waves, wavenumbers $k = -20$ to -5 and periods between 2.5 and 10 days are considered.

EOFs are calculated using the covariance matrix of filtered T_b over different domains described in Table 1. Then, analysis is based on linear regressions following a similar procedure from previous works (Kiladis et al. 2016; Snide et al. 2022; Mayta and Adames 2023). Briefly, the principal component (PC) time series of the first EOF mode for the TD-like and equatorial Rossby waves are used to calculate the linear regression. The dynamical fields associated with each corresponding wave are obtained by projecting unfiltered reanalysis fields at each grid point onto the associated time series. The perturbations are scaled to one standard deviation of the corresponding PC perturbation. Finally, the statistical significance of these results is assessed based on a two-tailed Student's t test that takes into account the correlation coefficients and an effective number of independent sample (degrees of freedom) based on the decorrelation time scale (Livezey and Chen 1983).

c. *Diagnostic criteria*

In this study, we apply the criteria documented in previous studies (e.g., Sobel and Bretherton 2003; Adames et al. 2019; Ahmed et al. 2021), and unified in Mayta et al. (2022) to investigate whether all the equatorial Rossby and TD-like waves satisfy the conditions to be considered as moisture modes. Following Mayta et al. (2022), the four criteria proposed to identify moisture modes can be summarized as follows.

C1: The wave must exhibit a large moisture signature that is highly correlated with the precipitation anomalies. For a tropical system to be considered a moisture mode, its signature in column water vapor ($\langle q' \rangle$) must be large enough to significantly modulate surface precipitation (P') as follows:

$$\langle q \rangle' \propto P' \tag{1}$$

where $\langle \cdot \rangle \equiv (1/g)\int_{100}^{1000}(\cdot)dp$ represents integration from 1000 to 100 hPa, and the prime ($'$) represents the regressed anomalies. This results in a strong correlation (~0.9 rounded) between P' and $\langle q \rangle'$, because in moisture modes column water vapor should largely explain the rainfall variance, defined as at least 80% in Mayta and Adames (2023).

C2: The wave must satisfy WTG balance at the leading order. The WTG approximation in the column-integrated dry static energy (DSE) budget can be expressed as

$$\nabla \cdot \langle s\mathbf{v} \rangle' \simeq \langle Q_1 \rangle', \tag{2}$$

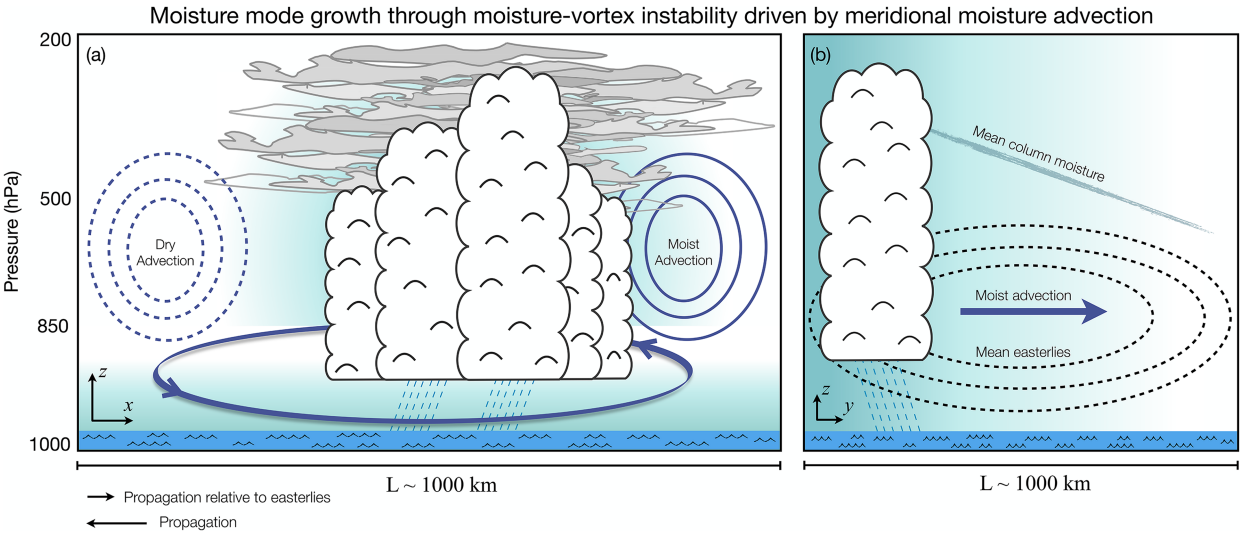

FIG. 2. Schematic depiction of the structure of a moisture mode that grows from moisture vortex instability (MVI). (a) Longitude–height view of the system. (b) Latitude–height cross section of the rightmost portion of (a). In (a), clouds denote the region of active precipitation, the thick line with arrows denotes the horizontal circulation, and the thinner solid contours denote anomalous southerly winds while the dashed contours denote the anomalous northerlies. In (b), the dashed contours denote the mean easterlies while the arrow shows the direction of anomalous moisture. In both panels, the background shading describes the humidity.

where $s = C_pT + \phi$, $\mathbf{v} = u\mathbf{i} + v\mathbf{j}$ is the horizontal vector wind field. $\langle Q_1\rangle' \simeq \langle Q_r\rangle' + L_vP' + \mathrm{SH}'$ is the apparent heating rate and can be estimated as in Mayta et al. (2022), where Q_r is the column radiative heating rate, SH is the surface sensible heat flux, and L_v is the latent heat of vaporization (2.5×10^6 J kg^{-1}). Considering that spatial and temporal variations in temperature are small over tropics, the left hand of Eq. (2) is equivalent to $\omega\partial_p s$.

On their own, C1 and C2 may be considered sufficient conditions to determine whether a system is a moisture mode. However, C2 can indicate that $\langle Q_1'\rangle$ is very large, and not that temperature fluctuations are negligibly small. As a result, we may have systems that satisfy C2 in which temperature plays a comparable role to moisture in their thermodynamics. Adames (2022) showed that such systems are possible and referred to them as mixed systems. Thus, additional criteria are necessary to confirm that the temperature fluctuations are indeed negligible compared to the moisture anomalies.

C3: Thermodynamic variations in the wave must be dominated by moisture. Moisture modes occur when moisture governs the distributions of anomalous MSE:

$$\langle m\rangle' \approx L_v\langle q\rangle', \tag{3}$$

where $m = s + L_vq$ is the moist static energy (MSE).

C4: N_{mode}. This dimensionless parameter can quantify the relative importance of moisture versus temperature to any wave type and can be estimated following Adames et al. (2019):

$$N_{\mathrm{mode}} \simeq \frac{c_p^2\tau}{c^2\tau_c}, \tag{4}$$

where c is the phase speed of a first baroclinic free gravity wave ($c \simeq 50$ m s^{-1}), c_p is the phase speed of the wave, τ_c is the convective moisture adjustment time scale, defined as a measure of the sensitivity of precipitation to changes in moisture (Betts 1986), and $\tau = \lambda/c_p$ is the temporal time scale with λ being the wavelength. When $N_{\mathrm{mode}} \ll 1$, moisture governs the thermodynamics of a wave, resulting in moisture modes; but if $N_{\mathrm{mode}} \gg 1$ the thermodynamics of a wave are predominantly driven by temperature fluctuations, as in gravity waves. When $N_{\mathrm{mode}} \approx 1$ the wave will exhibit both moisture mode and gravity wave behavior.

3. Moisture–vortex instability

As discussed by Adames and Ming (2018a) and Adames (2021), MVI is the result of interactions between large-scale moistening driven by moisture and temperature advection, convection, and the wave's circulation. While MVI is not an instability that can occur strictly in moisture modes, solely focusing on these systems yields a simpler interpretation of this process.

Figure 2 shows the structure of a moisture mode that grows from MVI. The wave is characterized by an anomalous low-level cyclone with lower-tropospheric northerlies to its west and easterlies to its east (Fig. 2a). In most regions of the Northern Hemisphere tropics, the northerlies will advect dry air and the southerlies will advect moist air as a result of the climatological-mean MSE gradient (Fig. 2b). Thus, moistening occurs to the east of the wave axis and drying occurs to the west. Precipitation does not occur where the moistening is a maximum. Rather, it occurs where the anomalies in column-integrated water vapor are the largest. This distinction is crucial to MVI: there is a delay between the large-scale moistening and the precipitation, allowing convection to develop closer to the vortex center. In the case of the wave shown in Fig. 2, the convection will be a maximum slightly to the east

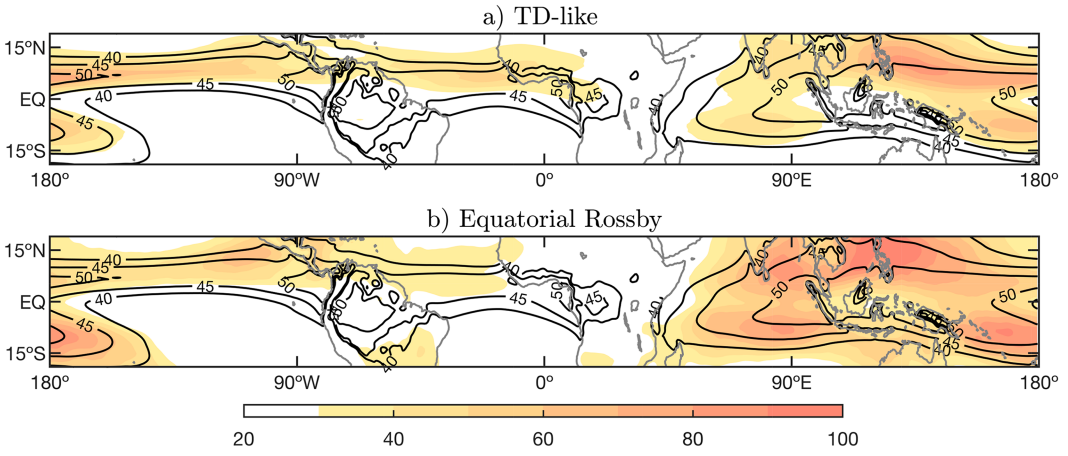

FIG. 3. Geographical distribution of the variance of (a) TD-like and (b) equatorial Rossby wave-filtered CLAUS T_b for all seasons. Shading intervals in K^2 are shown at the bottom of the plot. Contours in both panels indicate the all-season mean of total column water vapor.

of the vortex center. Vortex stretching arising from the convection will result in eastward propagation relative to the prevailing easterly winds, as well as vortex amplification.

In summary, systems that grow from MVI should exhibit the following features:

F1: A high coherence between anomalous moisture and precipitation (moisture mode criterion C1).
F2: Lower tropospheric convergence must have an in-phase component with the lower-tropospheric streamfunction, implying growth from vortex stretching.
F3: Advection of mean moisture by the anomalous winds must contribute to the growth of the moisture anomalies.

All of these features are examined in the following sections.

4. Large-scale features of the TD-like and equatorial Rossby waves

a. *Filtered variance of TD-like waves and equatorial Rossby waves*

Figure 3 shows a map of T_b variance filtered to retain TD-like and equatorial Rossby wave activity only. The variance maps show that the maximum activity of both TD-like and equatorial Rossby waves occurs in off-equatorial regions where the column moisture gradient is steep rather than where column moisture is the largest. Such a result indicates that these waves occur in regions where MVI is possible, a possibility that is examined below. The preference for strong meridional moisture gradients is evident in the correlations between filtered T_b and column moisture and column moisture meridional gradient, respectively, as shown in Table A1. We also argue that the off-equatorial nature of moisture modes arises from the need for a planetary vorticity that is substantially larger than zero in magnitude.

Based on this variance map, we will perform EOF analysis in four regions where TD-like activity is a maximum. As shown in Table 1, these regions are located in the Atlantic, eastern Pacific, western Pacific, and the Indian Ocean. For the equatorial Rossby waves, EOF analyses are performed in three regions considering the maximum variance of the equatorial Rossby wave shown in Fig. 3. The regions are the eastern Pacific-Atlantic basin, the western Pacific, and the Indian Ocean (Table 1).

b. *TD-like waves across the tropics*

Before examining the moist thermodynamics of TD-like waves, we first investigate variations in the TD-like wave life cycle as a function of geographical variations. Figure 4 shows the horizontal structure of the 850-hPa circulation projected onto PC1 TD-filtered T_b over different regions at lag day 0. Table 1 summarizes the different regions considered for EOF calculation based on the maximum variance observed in Fig. 3a.

For the TD-like wave over the Atlantic region, PC1 and PC2 together explain about ~20% of the filtered variance and describes the wave activity over western Africa and tropical Atlantic region (Fig. 4a). The circulation pattern associated with this disturbance closely resembles those previously documented over Africa and the Atlantic Ocean (e.g., Kiladis et al. 2006). Over the Atlantic region, these waves propagate at ~8.6 m s^{-1}. Similar structure and phase speed were documented recently in Mayta and Adames (2023) by using principal component analysis calculated in a broader region.

Figure 4b presents the circulation features for TD-like waves over the eastern Pacific. Despite the circulation and convection evolution being shown throughout the entire year, the observed structure closely resembles those Pacific easterly waves documented in many previous works (Serra et al. 2010; Rydbeck and Maloney 2014, 2015; Huaman et al. 2021). Positive anomalies of moisture move into the trough as the wave propagates toward the west (Fig. 4b). As the waves propagate westward at about 7.3 m s^{-1}, the wave shows the characteristic southwest-northeast tilt, similar to the TD-like waves over the Atlantic region. Such a tilt implies that barotropic energy

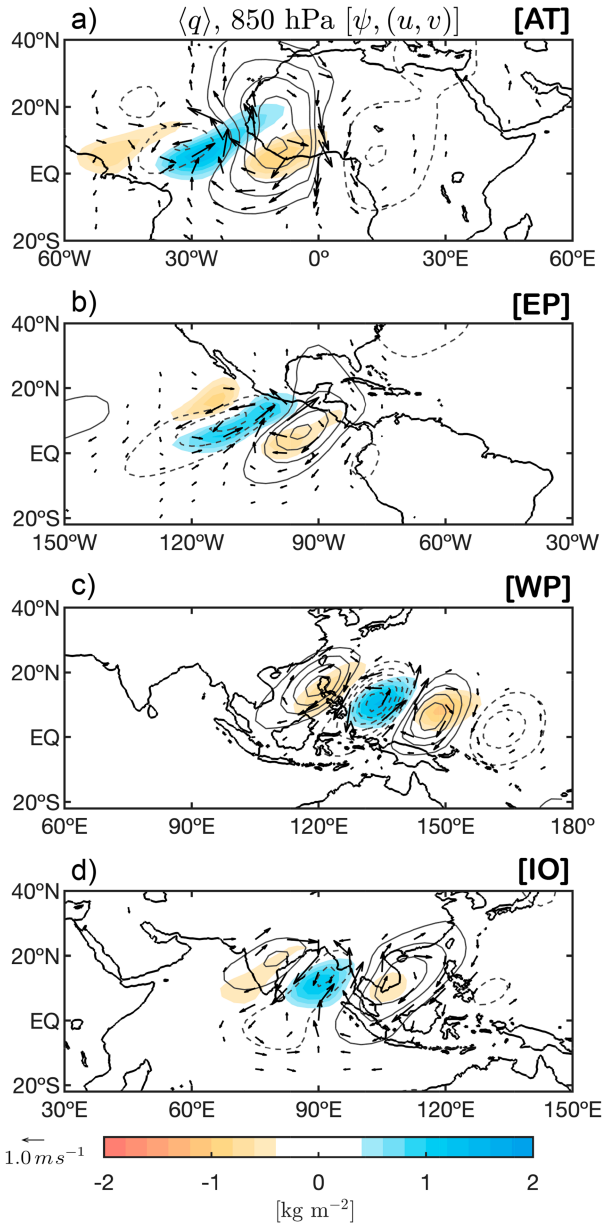

FIG. 4. Anomalous column moisture (shading), 850-hPa streamfunction (contours), and 850-hPa winds (vectors) regressed onto PC1 TD-like wave-filtered T_b on day 0 in different oceanic regions of the tropics: (a) Atlantic (AT; 0°–15°N, 60°W–0°), (b) eastern Pacific (EP; 5°–20°N, 120°–80°W), (c) western Pacific (WP; 0°–15°N, 110°–160°E), and (d) Indian Ocean (IO; 0°–15°N, 70°–100°E). All fields are scaled to one standard deviation PC perturbation of the TD-like wave. Streamfunction contour interval is 1.0×10^6 m^2 s^{-1}, with negative contours dashed. Shading and contours indicate regions significant at the 95% level. Wind vectors are plotted only where either the u or v component is significant at the 99% level or greater.

conversions may play a role in these systems (e.g., Rydbeck and Maloney 2014).

The leading pair of PCs of filtered T_b over the western Pacific explain ~22% of the total filtered variance. Figure 4c shows the evolution of the horizontal structure of TD-like wave at 850 hPa level. At this level, alternating cyclonic and anticyclonic gyres are observed within the positive and negative columns of water vapor anomalies, respectively. This higher column moisture is also collocated closer to the center of the trough or low pressure, consistent with the MVI's feature F2 described in section 3. Northwestward propagation can be inferred from the equatorial western Pacific toward the Philippines Sea and southeastern China as documented in previous studies (e.g., Lau and Lau 1990; Kiladis et al. 2009; Feng et al. 2020). The wave propagates at about 5.8 m s^{-1}, slightly slower than the TD-like waves over other regions. This is likely because of the weaker mean-flow advection in this region, which is the dominant component of the phase speed and group speeds of these TD-like disturbances (e.g., Sobel and Horinouchi 2000).

Figure 4c shows the regressed horizontal structure by using PC1 of filtered T_b over the Indian Ocean, which explains about 20% of the variance. The anomalous anticyclone is followed by cyclonic gyres coupled with positive column water vapor anomalies (Fig. 4d). The enhanced moisture and circulation show its maximum amplitude around the Bay of Bengal and dissipates as the wave propagates toward the west-northwest at about 7.2 m s^{-1}. The horizontal structure presented in Fig. 4d closely resembles those previously documented for Indian monsoon low pressure systems (e.g., Hunt et al. 2016; Adames and Ming 2018b; and references therein).

c. *Equatorial Rossby waves across the tropics*

Figures 5a–c display the horizontal structure of the 850-hPa circulation projected onto PC1 of the equatorial Rossby wave.

For equatorial Rossby over the Atlantic region, PC1 and PC2 together explain 25% of the filtered variance and represent the equatorial Rossby wave activity over the tropical Atlantic and the eastern Pacific, in agreement with the geographical distribution of the maximum annual-mean equatorial Rossby variance (Fig. 3b). A detailed description of all features of this wave over the Western Hemisphere is documented in Mayta et al. (2022).

Equatorial Rossby waves over the west Pacific warm pool are presented in Fig. 5b. Over this region PC1 and PC2 together explain 26% of the filtered variance. The predominant zonal wavenumber of the circulation at this level is around k = 4–5. The characteristic cyclonic pair (stronger in the Northern Hemisphere) is apparent with circulation and convective features propagating westward at a phase speed of 5.9 m s^{-1}. Despite the circulations being more equatorially trapped like the theoretical wave structure, there is some indication of connections to the extratropics in both hemispheres. Similar features of this wave were documented in previous studies (e.g., Wheeler et al. 2000; Kiladis et al. 2009; Gonzalez and Jiang 2019).

Over the Indian Ocean region, PC1 and PC2 together explain 15% of the filtered variance. Overall, the wave structure varies according to the season (not shown), but Fig. 5c is representative of the annual-mean equatorial Rossby wave. Unlike other tropical regions, the positive anomalies of column

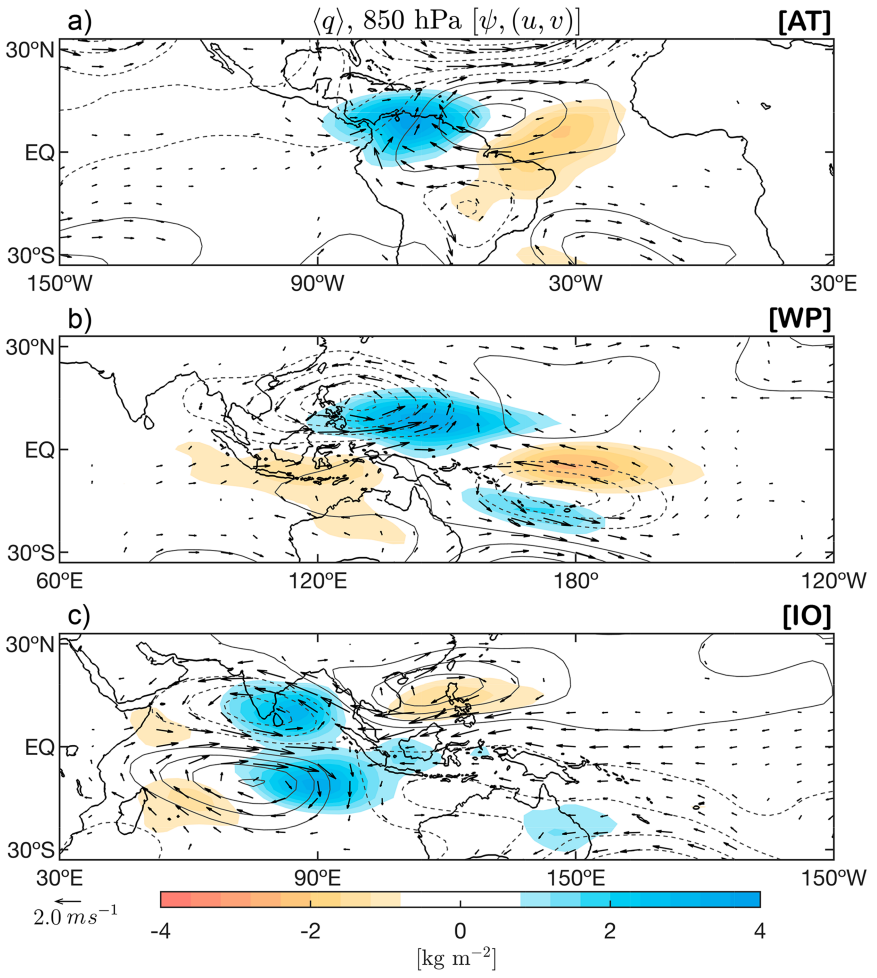

FIG. 5. As in Fig. 4, but regressed onto PC1 equatorial Rossby wave at lag day 0. EOFs were computed in different regions of the tropics: (a) Atlantic (AT; 5°S–25°N, 125°W–0°), (b) western Pacific (WP; 25°S–25°N, 110°E–150°W), and (c) Indian Ocean (IO; 20°S–25°N, 50°–110°E). All fields are scaled to one standard deviation PC perturbation of the equatorial Rossby wave. Streamfunction contour interval is 2.0×10^6 m^2 s^{-1}, with negative contours dashed. Shading and contours indicate regions significant at the 95% level. Wind vectors are plotted only where either the u or v component is significant at the 99% level or greater.

water vapor and circulation features closely resemble the theoretical Rossby wave structure over the Indian Ocean (Matsuno 1966). A quasi-symmetric pair of cyclonic gyres is clearly visible in Fig. 5c. In addition, an equatorial easterly wind perturbation to the east of the region of maximum convection resembles the Kelvin response to equatorial heating (Gill 1980). Over the Indian Ocean, equatorial Rossby waves are sufficiently long-lasting and propagate slowly enough (at about 3.9 m s^{-1}; see Table 3) to force a "Gill-type" response, as in the MJO.

5. Governing thermodynamics

We now examine criteria C1 to C3 by constructing scatterplots as shown in Fig. 6. For C1 the slope of the linear fit gives the value of the convective moisture adjustment time scale ($\tau_c = \langle q' \rangle / P'$). Previous studies have found that τ_c varies from 6 to 24 h over the rainy regions of the tropics (e.g., Betts and Miller 1993; Bretherton et al. 2004; Sobel and Maloney 2012; Jiang et al. 2016; Adames and Kim 2016). In addition, Adames et al. (2019) suggested that τ_c must be longer than 12 h (0.5 days) to guarantee a large moisture signature in moisture modes (see their Fig. 3), which is also seen in this work. The values of τ_c and the correlation coefficient for TD-like and equatorial Rossby waves over different tropical regions are summarized in Table 2. The results show that TD-like waves pass the first criterion in our four regions of interest, with correlations ranging from ~0.88 to ~0.97 and τ_c greater than 0.5 days.

The same behavior is found for the equatorial Rossby wave. As seen in Fig. 6d and Table 2, P' and $\langle q \rangle'$ show a strong correlation in all regions oscillating from ~0.88 to

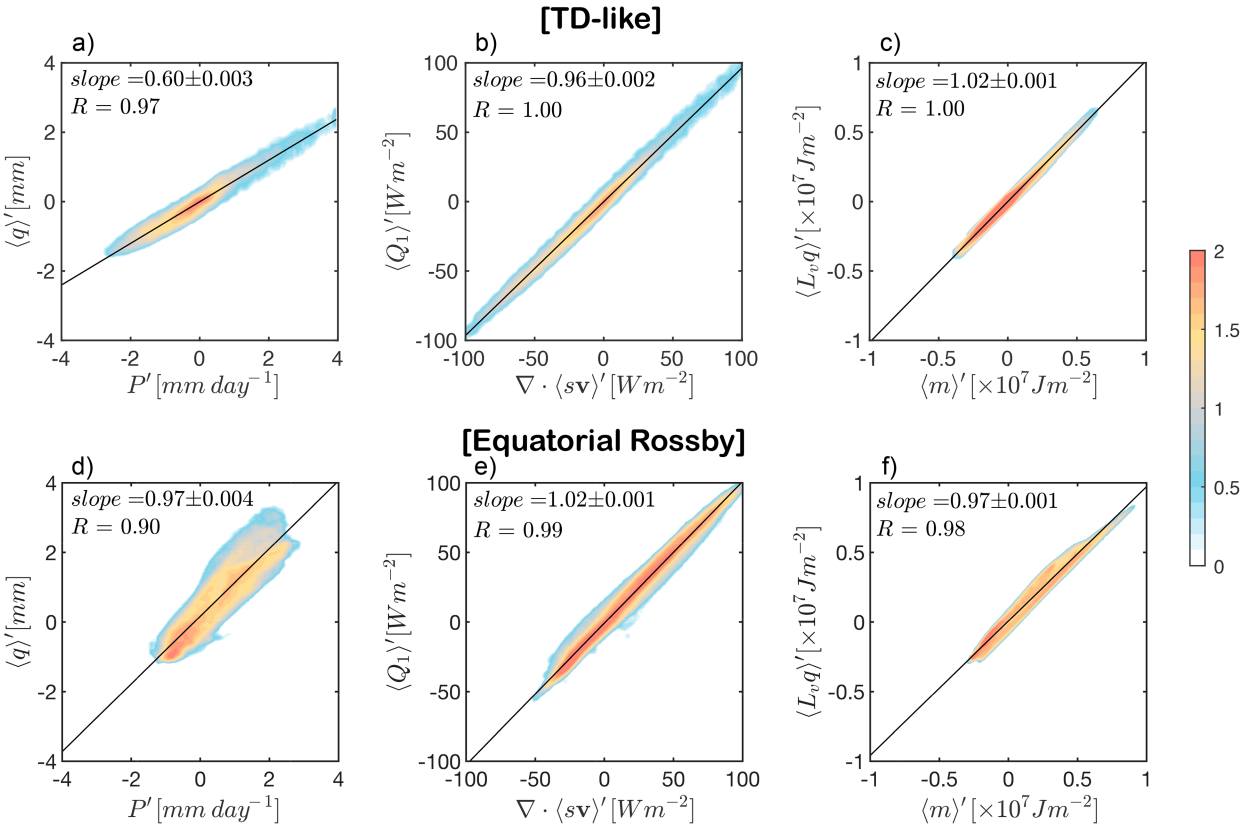

FIG. 6. Scatterplots of (a) P' vs $\langle q\rangle'$, (b) $\nabla\cdot\langle \mathbf{sv}\rangle'$ vs $\langle Q_1\rangle'$, and (c) $\langle m\rangle'$ vs $\langle L_v q\rangle'$ for the (top) TD-like wave and (bottom) equatorial Rossby wave. The shading represents the base-10 logarithm of the number of points within 0.1 mm × 0.1 mm bins in (a), 2.5 W m^{-2} × 2.5 W m^{-2} bins in (b), and 2.0 × 10^5 J m^{-2} × 2.0 × 10^5 J m^{-2} bins in (c). Anomalies are obtained by regressing all fields against PC1 time series of (top) TD-like waves over the western Pacific and (bottom) equatorial Rossby waves over the Indian Ocean region. The domain chosen for the criteria calculation is shown in Table 2. The linear fit obtained from linear least squares fit is shown as a solid black line. The slope of the linear fit and the correlation coefficient are shown in the top left of each panel.

~0.96. As also expected, equatorial Rossby waves show slow convective adjustments with τ_c oscillating on the order of 1.0 days and larger. These values broadly resemble previous findings (e.g., Yasunaga et al. 2019; Adames et al. 2019), where moisture dominance ($\tau_c \geq 0.5$ days) was found at low frequencies. As documented in Wolding et al. (2020b), small values of τ_c usually mean some other process is causing rainfall, leading τ_c to decrease. Furthermore, moisture modes rarely exist if the convective adjustment is short [see Ahmed et al. (2021) for more details].

For criterion C2 to be satisfied, the waves must exhibit a high correlation (~0.9 rounded) between $\nabla\cdot\langle \mathbf{sv}\rangle'$ and $\langle Q_1\rangle'$, and the slope must be within the margin of 0.9–1.1. From Figs. 6b and 6e and Table 2, we can see that the correlation between column DSE divergence and Q_1 is in close unity to all of the TD-like and equatorial Rossby waves. In addition,

TABLE 2. Moisture mode criteria applied to TD-like and ER waves over different tropical regions. The slope of the linear fit and the correlation coefficient are shown in a similar manner to Fig. 6. An asterisk (*) indicates that the values for the equatorial Rossby mode over the Atlantic region come from Mayta et al. (2022).

		C1: $P' \propto \langle q\rangle'$		C2: $\nabla\cdot\langle \mathbf{sv}\rangle' \simeq \langle Q_1\rangle'$		C3: $\langle m\rangle' \approx L_v\langle q\rangle'$	
Wave	Region	Slope	Corr	Slope	Corr	Slope	Corr
TD-like	Atlantic	0.60 ± 0.007	0.88	0.95 ± 0.003	0.99	1.06 ± 0.002	1.00
	Eastern Pacific	0.51 ± 0.003	0.94	0.98 ± 0.002	1.00	1.07 ± 0.003	0.99
	Western Pacific	0.60 ± 0.003	0.97	0.96 ± 0.002	1.00	1.02 ± 0.001	1.00
	Indian Ocean	0.53 ± 0.003	0.90	0.89 ± 0.003	0.97	1.06 ± 0.002	0.99
Equatorial Rossby	E. Pacific–Atlantic*	1.63 ± 0.007	0.96	0.99 ± 0.002	0.99	1.04 ± 0.002	0.99
	Western Pacific	0.91 ± 0.003	0.88	0.98 ± 0.001	1.00	0.89 ± 0.001	0.98
	Indian Ocean	1.04 ± 0.004	0.90	1.02 ± 0.001	0.99	0.97 ± 0.001	0.98

TABLE 3. N_{mode} values for TD-like and Rossby waves. The phase speed (c_p) is calculated by applying a Radon transform [more details in Mayta et al. (2021) and Mayta and Adames (2021)]. The convective moisture adjustment time scale (τ_c) is estimated as the slope of the linear fit in the scatterplot of Fig. 6. An asterisk (*) indicates that the values for the equatorial Rossby mode over the Atlantic region come from Mayta et al. (2022).

Wave	Region	c_p (m s^{-1})	τ (days)	τ_c (days)	N_{mode}
TD-like	Atlantic	8.6	5.2	0.60	0.24
	Eastern Pacific	7.3	5.0	0.51	0.21
	Western Pacific	5.8	6.0	0.60	0.13
	Indian Ocean	7.2	5.2	0.53	0.20
Equatorial Rossby	E. Pacific–Atlantic*	5.4	13.7	1.63	0.10
	Western Pacific	5.9	17.5	0.91	0.23
	Indian Ocean	3.9	24.5	1.04	0.14

the slope of the linear least squares fit of the two fields is ~1 in both disturbances.

Figures 6c and 6f show a scatterplot of $\langle m \rangle'$ versus $L_v \langle q \rangle'$ with the least squares fit. We see that the slope of the linear fit is ~1 for the TD-like and equatorial Rossby waves over the Indian Ocean. It is also fulfilled in the other studied basins (Table 2). When C1, C2, and C3 are examined together, we see that both TD-like and equatorial Rossby waves pass the three criteria across all tropical oceans and therefore can be considered moisture modes.

In addition to the three aforementioned criteria, we utilized the nondimensional number N_{mode} as an additional criterion. Table 3 shows the values of the parameters in Eq. (4) along with the obtained value of N_{mode}. For the TD-like waves, the largest value of N_{mode} is seen over the Atlantic region, with a value of ~0.24. Through this region, the wave propagates slightly faster compared to the other regions with a phase speed of ~8.6 m s^{-1}. TD-like waves over the eastern Pacific and over the Indian Ocean (Bay of Bengal) show approximately the same N_{mode} value of 0.21 and 0.20, respectively. With a value of 0.13, TD-like waves over the western Pacific exhibit the lowest value of N_{mode}, largely due to their slower propagation speed of ~5.8 m s^{-1} which in turn depends on the mean flow, via advection. Equatorial Rossby waves, on the other hand, have N_{mode} values that are much smaller than unity ($N_{\text{mode}} \sim 0.1$) over the three basins assessed in this study. Compared with TD-like waves, equatorial Rossby waves propagate slower at about 4–5 m s^{-1}. Over the western Pacific, the wave propagates slightly faster at 6 m s^{-1}, which results in a larger N_{mode} value of ~0.23 (Table 3).

Although the results shown in Table 3 are useful, it is worth noting that these values are the result of a restrictive analysis. To further analyze moisture modes along the tropics, the space–time spectral distribution of N_{mode} is calculated and compared with the typical dispersion curves of convectively coupled equatorial waves, as in Adames (2022) and Mayta and Adames (2023). From an examination of Fig. 7 we see that TD-like and equatorial Rossby waves fall well within the moisture mode domain of the N_{mode} spectrum (blue regions). Although most of the TD-like T_b spectrum falls into the blue region, a portion of the signal falls into the white region that corresponds to mixed systems.

6. Vortex stretching in moisture modes

In Figs. 4 and 5 we see that the $\langle q \rangle$ anomalies are close to in phase with the lower tropospheric streamfunction anomalies, consistent with feature F2 of MVI. This result suggests that vortex stretching contributes to the growth of these systems. We can examine this more objectively by employing the same projection techniques utilized in previous studies (e.g., Andersen and Kuang 2012; Arnold et al. 2015; Adames 2017; among others):

$$\text{Proj}(X, Y) \equiv \frac{\int\int XY \, dA}{\int\int Y^2 \, dA}, \tag{5}$$

where the area-weighted sum is taken over the domains of the corresponding waves detailed in Table 1. The lags used for the calculation represent the different stages of equatorial Rossby (lag days between −8 and +8) and TD-like waves (lag days between −2 and +2). The area considered for TD-like waves and the equatorial Rossby waves are the same region used for the EOF calculation detailed in Table 1. The chosen area represents the region where the waves are most active (Figs. 4 and 5).

From the examination of Fig. 8, it is evident that low-level divergence is at least partly in phase with the streamfunction at all lags. In both cases, the maximum amplitude occurs before the peak convection. The phase relationship between convergence and streamfunction implies that all the moisture modes documented in this study exhibit feature F2.

7. MSE budget analysis

Since the anomalous convection of TD-like and Rossby waves is closely tied to the column MSE (e.g., Figs. 4–6), an examination of the MSE budget can provide valuable insights into the processes that control the convection evolution of moisture modes.

The column-integrated MSE budget is defined as in Yanai et al. (1973):

$$\frac{\partial \langle m \rangle'}{\partial t} = -\langle \mathbf{v} \cdot \nabla_h m \rangle' - \left\langle \omega \frac{\partial m}{\partial p} \right\rangle' + \langle Q_r \rangle' + \underbrace{L_v E' + \text{SH}'}_{\text{SF}'}, \tag{6}$$

where $m \equiv s + L_v q$ is MSE, $\mathbf{v} = u\mathbf{i} + v\mathbf{j}$ is the horizontal vector wind, and $\nabla_h \equiv \mathbf{i}\partial/\partial x + \mathbf{j}\partial/\partial y$ the horizontal gradient. The

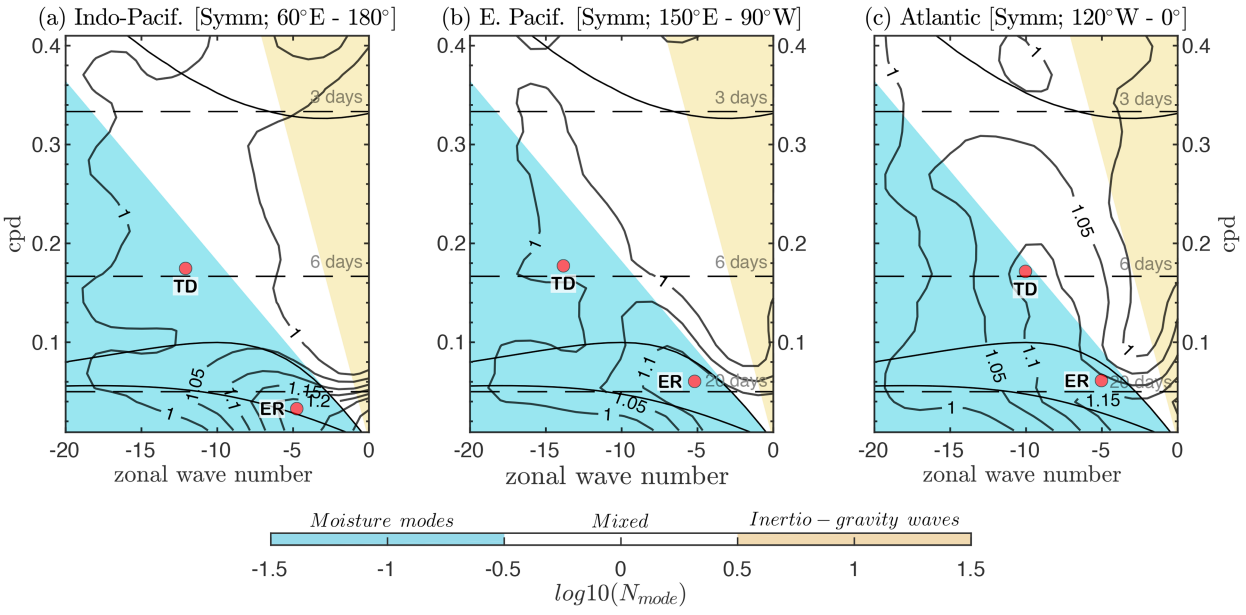

FIG. 7. Regional wavenumber–frequency power spectrum (contours) of the symmetric component of CLAUS T_b calculated for three different regions of the tropics between 10°N–10°S: (a) Indo-Pacific (60°E–180°), (b) eastern Pacific (150°E–90°W), and (c) Atlantic (120°W–0°). The solid dispersion curves correspond to 8 and 70 m equivalent depths. The functional form of the tapering window is the same as described in Wheeler and Kiladis (1999). Background spectra were estimated separately for the regional domain, using the smoothing procedure of Dias and Kiladis (2014). Contour interval is 0.05. Shadings represent wavenumber–frequency distribution of base 10 logarithm of N_{mode} following a similar procedure of Adames (2022). Blue shading represents tropical systems that can be categorized as moisture modes, yellow can be considered inertio-gravity waves, and white represents mixed systems. Orange circles approximately represent the average zonal wavenumber and frequency of the corresponding TD-like and Rossby wave for the different regions.

left-side term in Eq. (6) is the MSE tendency. The first and second terms on the right-hand side of Eq. (6) represent horizontal MSE advection and vertical MSE advection, respectively. The other terms on Eq. (6) are MSE source terms: the radiative heating rate, surface latent heat flux (L_vE), and surface sensible heat flux (SH). The L_vE' and SH′ terms are analyzed together as surface fluxes (SF′).

Considering that advective processes play an important role in the propagation and growth of slow-moving disturbances (e.g., Mayta et al. 2022), it is instructive to decompose this process into the following contributions (Fig. 9):

$$-\langle \mathbf{u}\nabla m\rangle \approx -\langle \overline{\mathbf{u}}\nabla m'\rangle - \langle \mathbf{u}'\nabla \overline{m}\rangle - \langle \mathbf{u}'\nabla m'\rangle, \qquad (7)$$

where $\mathbf{u} = u\mathbf{i} + v\mathbf{j} + \omega\mathbf{k}$ is the vector wind field and $\nabla \equiv \mathbf{i}\partial/\partial x + \mathbf{j}\partial/\partial y + \mathbf{k}\partial/\partial p$ is the gradient operator in isobaric coordinates. The overbar represents the low-frequency component, obtained from a 30-day low-pass filter, and the primes are departures from this low-frequency component.

In addition, following Eq. (5), we estimate the processes that lead to the propagation and growth of the moisture modes by projecting each MSE budget term upon the MSE tendency and the MSE anomalies, respectively. The contributors to tendency can be interpreted as the mechanism responsible for the propagation of the wave. Conversely, the contribution to growth can also be understood as increasing MSE variance. For a process to contribute to the growth of MSE anomalies, it must be at least partially in phase with these anomalies.

Figure 9 shows the contribution to the propagation and growth of the TD-like and equatorial Rossby waves. It is an average of the three regions shown in Table 1. Each corresponding basin is displayed in Figs. S1–S4 in the online supplemental material. Each bar represents a time lag, ranging from lag day −2 (−8) to +2 (+8) in TD-like (equatorial Rossby) waves, with the day of maximum wave activity shown as a red circle.

The overwhelming contribution to the MSE tendency for TD-like waves comes from horizontal MSE advection. When we decompose the advection following Eq. (7), we find that the meridional advection of background MSE by the anomalous winds ($-\langle v'\partial_y \overline{m}\rangle$) and the advection of the MSE anomalies by the mean zonal wind ($-\langle \overline{u}\partial_x m'\rangle$) govern the propagation of the TD-like wave, contributing to over 75% of the column MSE tendency. Other terms contribute little to wave propagation.

As expected for slow-propagating disturbances, longwave radiative heating $\langle Q_r\rangle'$ contributes significantly to the growth of the TD-like waves, while vertical MSE advection damps it (Fig. 9b). A further decomposition of vertical MSE advection term indicates that the dominant vertical advection is primarily attributed to the advection of mean MSE by anomalous vertical velocity ($-\langle \omega'\partial_p \overline{m}\rangle$). The near cancellation between vertical MSE advection and radiative heating can be interpreted as a result of the upper-level clouds that result from deep convection, which suppresses longwave radiative cooling and compensate for the drying from vertical MSE advection (Adames and Ming 2018b; Inoue et al. 2020).

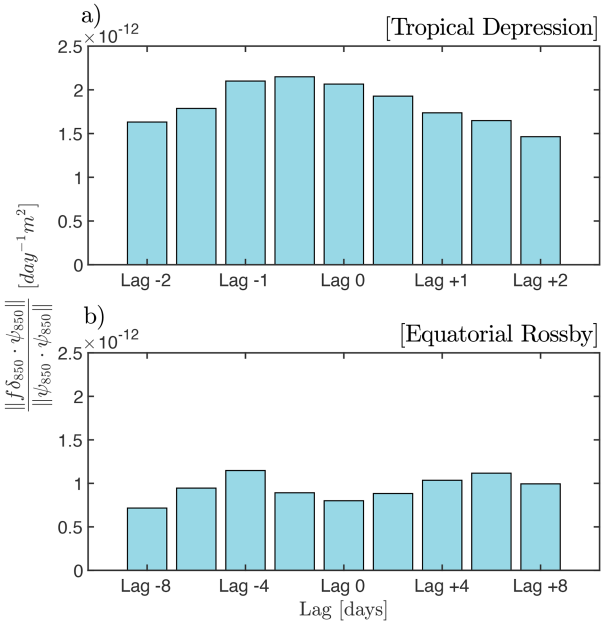

FIG. 8. Area-weighted projection of the anomalous low-level divergence (δ_{850}) onto streamfunction anomalies (ψ_{850}) for the (a) TD-like waves and (b) equatorial Rossby waves. Each bar represents the average value of all TD-like and equatorial Rossby waves at various time lags, ranging from lag day −2 to day +2 and from lag day −8 to day +8, respectively.

Although $\langle Q_r\rangle'$ and $-\langle\omega'\partial_p\overline{m}\rangle$ are the largest contributors to the growth and decay of the waves, their contributions do not change in time. Thus, they cannot explain the growth and decay of column MSE in TD-like and equatorial Rossby waves. Instead, it is the horizontal MSE advection that shows an evolution that is more consistent with this growth and decay. Specifically, the advection of mean moisture by anomalous meridional winds ($-\langle v'\partial_y\overline{m}\rangle$) contributes to the growth of TD-like waves (Fig. 9b), consistent with MVI feature F3 in section 3. In contrast, $-\langle\overline{u}\partial_x m'\rangle$ contributes to the decay of the TD-like wave. TD-like waves over the western Pacific region are one exception (Fig. S2c), where $-\langle\overline{u}\partial_x m'\rangle$ contributes to the growth and decay of the wave before and after the peak of convection, respectively. These results are likely due to spatial differences in the mean state $\overline{u}$ across the different basins. Horizontal MSE advection by high-frequency eddies, specifically the meridional component ($-\langle v'\partial_y m'\rangle$), act to dampen the MSE anomalies (Fig. 9b).

The processes that propagate and maintain the MSE anomalies in equatorial Rossby waves are similar to those that propagate and maintain the TD-like waves. However, some differences exist in the mechanisms responsible for the propagation of the equatorial Rossby waves. While $-\langle v'\partial_y\overline{m}\rangle$ and $-\langle\overline{u}\partial_x m'\rangle$ propagate the TD-like waves, $-\langle\overline{u}\partial_x m'\rangle$ alone contributes to about 50% of the MSE tendency (Fig. 9c). The same mechanism was recently documented in Mayta et al. (2022), who proposed that the wave propagates westward due to zonal moisture advection by the mean flow. As in TD-like waves, the major contributors to MSE maintenance are moisture transports by anomalous meridional winds and longwave radiative heating (Fig. 9d). The MSE terms that contribute to the decay of the wave are vertical advection and $-\langle\overline{u}\partial_x m'\rangle$. Only minor differences in these processes are seen across the different basins, as shown in the supplemental material.

8. Poleward eddy moisture fluxes in moisture modes

That the term $-\langle v'\partial_y\overline{m}\rangle$ acts to amplify the column MSE anomalies in all the waves examined here implies that v' and column water vapor are (at least) partly in phase in these systems. While this phase relationship is consistent with the MVI features described in section 3, it also implies that moisture modes flux anomalous moisture poleward (i.e., $\langle v'q'\rangle$ is poleward). To examine this possibility, we calculate the space–time spectral coherence and phase angle between 850 hPa v' and $\langle q'\rangle$. Unlike Fig. 7, we will show both eastward and westward-traveling waves and we will examine the Northern and Southern Hemispheres separately. This is done by following the cross-spectral analysis method outlined by Hayashi (1973, 1977). As in Adames et al. (2014) the coherence value at the 99% confidence interval is calculated to be 0.03.

When we examine the coherence squared between v' and $\langle q'\rangle$ (Fig. 10), we see that the most robust coherence values are seen in the westward-propagating moisture mode part of the spectrum in both hemispheres. The Northern Hemisphere has overall higher coherence values that extend to higher frequencies and zonal wavenumbers, likely due to the higher variance of activity in this hemisphere (see Fig. 3). The phase angle between v' and $\langle q'\rangle$, shown as arrows, reveals that poleward flow is associated with enhanced $\langle q'\rangle$ in both hemispheres. A slight tilt in the arrows (rightward and leftward in the Northern and Southern Hemispheres, respectively) indicates that the poleward flow is shifted eastward from the positive $\langle q'\rangle$ anomalies. This result is consistent with the finding that meridional MSE advection contributes to both the propagation and growth of the MSE anomalies, as shown in Fig. 9.

The aforementioned results are most robust for the coherence values that are found within the moisture mode region of the spectrum. Closer to the gravity wave part of the spectrum we see a phase angle in the opposite direction. The kink in the spectral signal in this region suggests that the signal here does not correspond to TD-like and equatorial Rossby waves, but rather to mixed Rossby–gravity waves.

We also see a strong coherence in eastward-propagating waves, with the maximum coherence centered near zonal wavenumbers 6–7 in both hemispheres. This signal is akin to the power spectrum found in midlatitude waves (Adames et al. 2014; Tulich and Kiladis 2021). They also transport moisture poleward, but their phase angle is different than those of moisture modes, and their coherence is not as high as those of moisture modes in the latitude belts of interest.

Last, it is worth noting that no statistically significant coherence is seen along the Kelvin wave band or any of the inertio-gravity waves. This result is expected since Kelvin waves do not have a meridional wind signature in the lower troposphere (Kiladis et al. 2009), but it is interesting that little

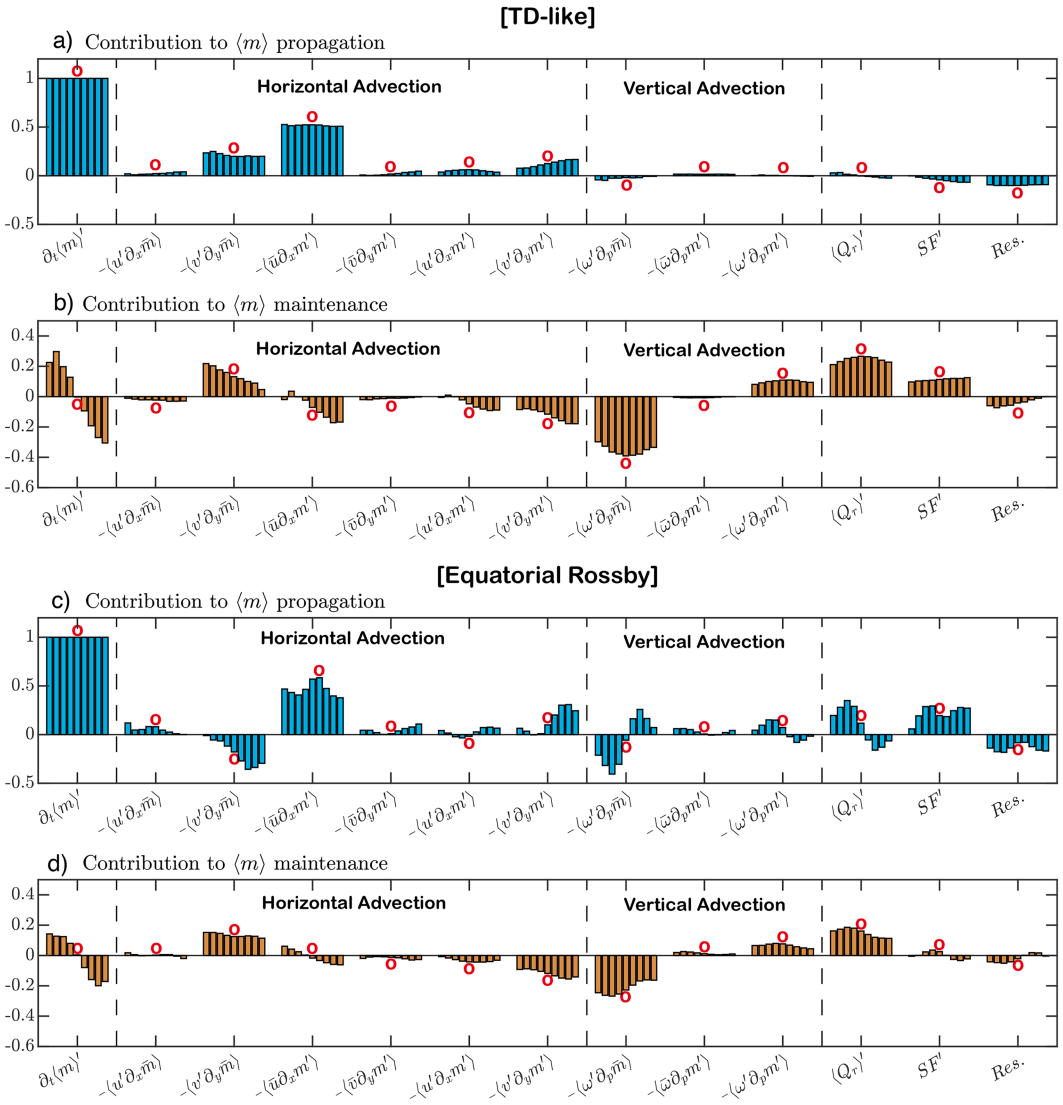

FIG. 9. The average contribution of each term in the MSE budget to the propagation (blue bars) and maintenance (brown bars) of the TD-like and equatorial Rossby waves obtained following Eq. (5). The contribution of each horizontal and vertical MSE advection term is delimited by dashed black lines. Red circles represent the peak of convection at the base point at day 0. The four bins before and after of peak of convection represent the lag regressions from day −2 to day +2 at every 12 h for TD-like waves and from day −8 to day +8 at every 2 days for equatorial Rossby waves.

coherence is seen in the gravity waves. It is also intriguing that the coherence between v' and $\langle q'\rangle$ along the MJO band is small.

A more direct examination of the meridional eddy moisture flux can be obtained from the lag regression fields shown in Figs. 8 and 9. The result, shown in Fig. 11, reveals that both TD-like and ER waves transport moisture poleward throughout most of their cycle. It is only slightly negative before lag day −4 for ER waves and lag day −1 for TD-like waves. After that day the transport quickly increases, reaching a peak amplitude at lag day 0.5 for TD-like waves and lag day 2 for ER waves. The positive lag in peak transport suggests that peak poleward moisture transport occurs after peak wave activity.

9. Summary and conclusions

This study is motivated by increasing evidence that a variety of moisture modes exist within the tropics, even outside of the warm pool, as hypothesized by Adames et al. (2019), Inoue et al. (2020), and Adames (2021). Mayta et al. (2022) found that equatorial Rossby waves over the Western Hemisphere satisfy all criteria to be considered a moisture mode. Mayta and Adames (2023) expanded upon this work and

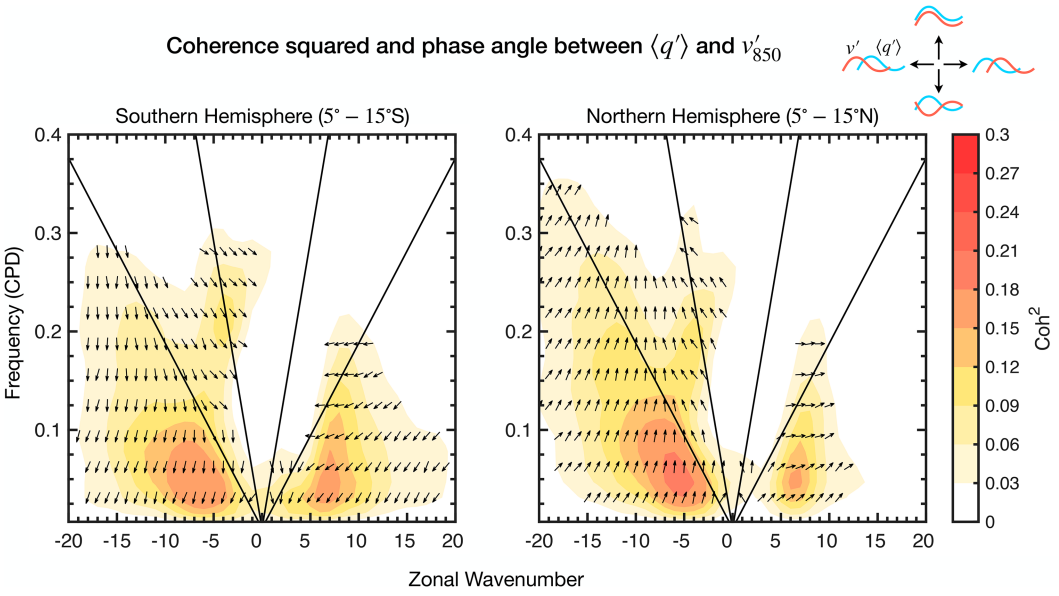

FIG. 10. Coherence squared (shading) and phase angle (vectors) between column moisture ($\langle q' \rangle$) and 850-hPa meridional wind (v'_{850}) for the (left) 5°–15°N and (right) 5°–15°S latitude belts. In both plots, the solid lines denote the transition lines from moisture modes to mixed systems (lower line) and from a mixed system to gravity wave (top line), as in Fig. 7. A guide to interpreting the phase angle is shown on the top right.

showed that Atlantic TD-like waves also satisfy the criteria to be classified as a moisture mode. Based on these results, we hypothesized that equatorial Rossby waves and TD-like waves are moisture modes, as predicted by the theory (Adames 2022). We examined a series of diagnostic criteria and the governing processes responsible for the growth and propagation of moisture modes by using ERA5 data. To investigate TD-like waves and equatorial Rossby waves, we computed an EOF analysis considering the maximum variance over different tropical regions (see Table 1 and Fig. 12). These indices were used to create lag regressions that elucidated the structure of the waves and their governing thermodynamic processes.

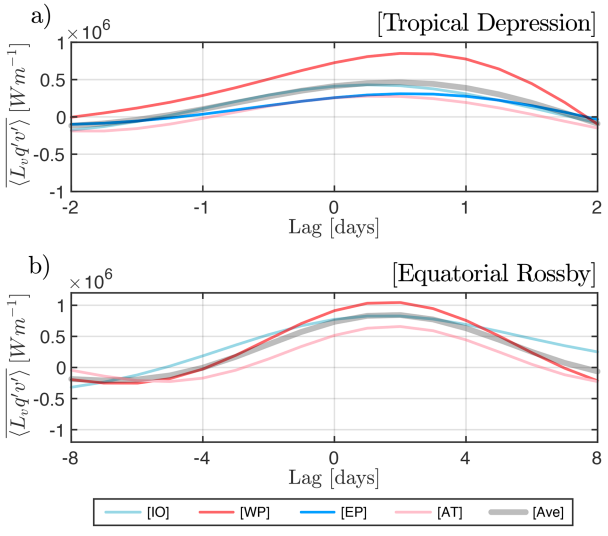

FIG. 11. Lag regression composite of area-averaged meridional eddy moisture flux ($\overline{\langle L_v q' v' \rangle}$). Time lag ranges from lag day −2 to day +2 for TD-like waves and from lag day −8 to day +8 for equatorial Rossby waves.

The composite dynamical structures, convection, and propagation features of TD-like and equatorial Rossby waves over the entire tropical domain (Figs. 4 and 5) depict an evolution that agrees with previous observational studies (e.g., Lau and Lau 1990; Takayabu 1994; Wheeler and Kiladis 1999; Kiladis et al. 2009; Rydbeck and Maloney 2014; Kiladis et al. 2016; Adames and Ming 2018b; Gonzalez and Jiang 2019; Feng et al. 2020; Mayta et al. 2022; Mayta and Adames 2023; among others).

By using the four criteria to identify moisture modes, we found that equatorial and off-equatorial moisture modes exist over the whole tropics (Fig. 6 and Table 2). The existence of these two moisture modes was initially predicted by theory (Adames et al. 2019; Adames 2022; Mayta et al. 2022), and their existence was confirmed over the Western Hemisphere (Mayta et al. 2022; Mayta and Adames 2023). Idealized model simulations also found the same results (e.g., Rios-Berrios et al. 2023). These two waves also exhibit an N_{mode} (a nondimensional number that measures the relative contribution of moisture and temperature in the evolution of moist enthalpy; Adames et al. 2019; Adames 2022) that is much smaller than unity over the entire tropical domain, another requirement necessary to be categorized as a moisture mode (Table 3). These features were also found in the space–time spectral

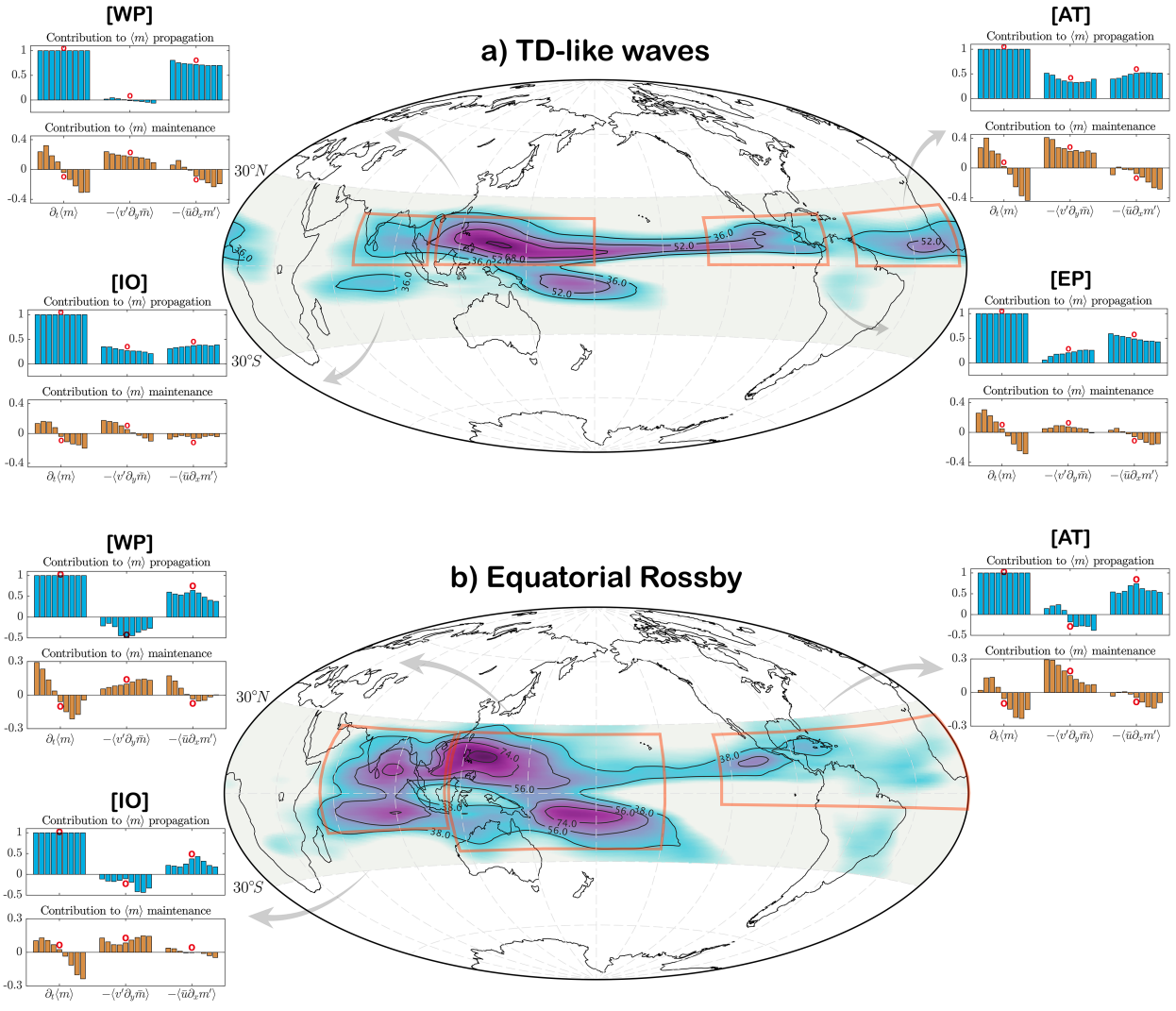

FIG. 12. Schematic depiction that shows the relative contribution of the meridional advection of background MSE by the anomalous winds ($-\langle v'\partial_y\overline{m}\rangle$) and the advection of the MSE anomalies by the mean zonal wind ($-\langle\overline{u}\partial_x m'\rangle$) to the propagation and growth of the MSE anomalies in the (a) TD-like and (b) equatorial Rossby waves. Blue and brown bars represent the process responsible for the propagation and maintenance of the moisture modes. The regions considered for the analysis of the TD-like and equatorial Rossby waves are represented by light red squares (see Table 1 for more details).

distribution of N_{mode} (Fig. 7). In the three basins considered for the analysis (Indian Ocean/western Pacific, central-eastern Pacific, and eastern Pacific/Atlantic), the centroid of the TD-like and equatorial Rossby wave signals falls within the moisture mode domain of the spectrum.

It is worth noting that, while most of the equatorial Rossby wave signal falls in the moisture mode region, a substantial portion of the TD-like wave signal is outside of this region N_{mode} spectrum (Fig. 7). Thus, not all TD-like waves are moisture modes. Faster-propagating TD-like waves have a larger value of N_{mode} and hence their temperature anomalies are expected to be larger. This is the case seen in African easterly waves, which were recently found to have an N_{mode} value between 0.3 and 0.5 (Vargas-Martes et al. 2023). While we do not examine AEWs in this study, recent observational and modeling studies (e.g., Wolding et al. 2020a; Núñez Ocasio and Rios-Berrios 2023) have shown that temperature fluctuations are as important as moisture in AEWs thermodynamics. In contrast to AEWs, most oceanic TD-like waves propagate slowly enough for gravity waves to eliminate temperature fluctuations before convection dissipates. This results in the dominance of moisture in the convective evolution of the wave that characterizes moisture modes (Adames 2022).

But where are these moisture modes most commonly found? A potential answer could be that these disturbances prevail in areas with the highest column water vapor. However, our results showed that moisture modes occur in regions with strong horizontal moisture gradients rather than in regions where moisture is maximum. This result is supported by the fact that the highest T_b variance in both equatorial Rossby

and TD-like waves is strongest in regions where the horizontal moisture gradient is strong (Fig. 3 and Table A1).

In light of these findings, our proposed answers to questions 1 and 2 in the introduction are as follows:

Q1: Moisture modes are common throughout the tropics.
Q2: Moisture modes preferentially occur in regions of strong horizontal moisture gradients.

In addition to the ubiquity of moisture modes found in this study, we also found that the propagation and growth of their MSE anomalies are governed by the same processes (Fig. 12):

1) The propagation of these moisture modes is governed by the advection of the MSE anomalies by the background trade winds, with an additional contribution from advection of background moisture by the anomalous meridional winds (Fig. 9). However, in the Indian Ocean equatorial Rossby waves, we found that anomalous surface fluxes contribute nonnegligibly to the propagation of the wave, more consistent with the results of Chen (2022).
2) While longwave radiative heating and vertical MSE advection are largely responsible for the growth and decay of slow-propagating moisture modes, they do not fully account for the temporal evolution of column MSE (Fig. 9 and supplemental figures). Instead, the horizontal MSE advection showed an evolution that is more consistent with the wave growth and decay. Especially, the growth of the MSE anomalies is the result of the advection of background moisture by the anomalous meridional winds (Fig. 12). Surface fluxes contribute nonnegligibly to TD-like waves' growth, which is not seen in equatorial Rossby waves. On the other hand, zonal moisture advection by the mean flow contributes to the decay of the wave (Figs. 9b,d). We argue that advection by mean flow contributes to wave decay because horizontal variations in the background zonal flow (not shown), drying the system during wave evolution. Last, the nonlinear meridional MSE advection term acts to dampen the TD-like waves in all of the regions examined. Equatorial Rossby waves are also damped by the same process but to a lesser extent. It is possible that nonlinear MSE advection may act as a type of diffusion, although more work is needed to better understand this finding.

But how are all these mechanisms related to moisture vortex instability? In section 3, we proposed three main features that systems should satisfy to grow from MVI (Fig. 2). Our results demonstrate that these features are prevalent in the equatorial Rossby and TD-like waves examined. These key characteristics can be summarized as follows:

F1: Moisture anomalies are in phase with the precipitation anomalies for oceanic TD-like waves and equatorial Rossby (C2; Fig. 6 and Table 2).
F2: Horizontal composite maps of column moisture and 850-hPa streamfunction of the moisture modes showed that moisture is roughly collocated with the cyclonic circulation (Figs. 4 and 5). Furthermore, lower-tropospheric convergence is partially in phase with the lower-tropospheric streamfunction, implying growth from vortex stretching (Fig. 6).
F2: Advection of background moisture by the anomalous meridional winds aids in the growth of moisture modes implying that the MSE anomalies grow from MVI (Sobel et al. 2001; Adames and Ming 2018a; Adames 2021).

Thus, our results indicate that the answer to question 3 in the introduction is as follows:

Q3: Moisture–vortex instability is present in oceanic TD-like waves and equatorial Rossby waves around the globe. This mechanism occurs in conjunction with growth by radiative heating.

Even though we have answered the three main questions of this study, our results lead to new questions. First, is there a reason why moisture modes appear to be common? Second, why does MVI appear to be so prevalent throughout the tropics? A hint to the answer can be seen in Figs. 10 and 11. Since v' and $\langle q' \rangle$ have an in-phase component, then moisture modes have a nonzero $\langle v'q' \rangle$, suggesting that they transport latent energy poleward. This appears to be the case in storm-permitting simulations of the tropics (Rios-Berrios et al. 2020) and even in reanalysis (Trenberth and Stepaniak 2003; Stoll et al. 2023). Thus, it is possible that moisture modes play an important role in tropical circulation. This possibility is examined within the context of a simplified model in Adames-Corraliza and Mayta (2024).

Acknowledgments. VM and ÁFAC were supported by NSF CAREER grant number 2236433 and by the University of Wisconsin startup package. VM and ÁFAC were also supported by NOAA grant number NA22OAR4310611. We thank George Kiladis for providing us with the CLAUS satellite data used in this study. ÁFAC would like to thank his late father, Ángel David Adames Tomassini, for listening to and motivating him to complete this project in spite of strenuous circumstances. VM would like to thank Chelsea Snide and the Large-scale Tropical Dynamics Group for helpful discussions throughout the course of this work. We also thank Prof. Adam Sobel and two anonymous reviewers for providing valuable comments that helped improve the contents of this manuscript.

Data availability statement. ERA5 data are available at https://www.ecmwf.int/en/forecasts/datasets/reanalysis-datasets/era5/. Interpolated T_b data are provided by NOAA/ESRL at https://catalogue.ceda.ac.uk/uuid/c2112bdd5f0ad698e70be6ab54c9a2ac.

APPENDIX

Is Moisture Mode Variance More Correlated with the Mean Moisture or the Mean Moisture Gradient?

To explore if strong moisture or meridional moisture plays an important role in the existence of moisture modes, we calculated the correlation between filtered T_b and the annual-mean column moisture and the mean meridional gradient of column moisture. The calculation is made based on

TABLE A1. Correlation of filtered T_b variance against moisture background ($\langle\overline{q}\rangle$); and meridional gradient of moisture background ($|\partial_y\langle\overline{q}\rangle|$). Correlations are calculated considering different basins based on Fig. 3. Note that $|\cdot|$ means absolute value.

Wave	Region	$\langle\overline{q}\rangle \propto T_b$	$\lvert\partial_y\langle\overline{q}\rangle\rvert \propto T_b$
TD-like	Atlantic (AT)	0.44	0.70
	Eastern Pacific (EP)	0.39	0.42
	Western Pacific (WP)	0.38	0.47
	Indian Ocean (IO)	0.50	0.60
Equatorial Rossby	Atlantic (AT)	0.28	0.45
	Western Pacific (WP)	0.41	0.32
	Indian Ocean (IO)	0.39	0.51

Fig. 3 and considering different basins. Table A1 summarizes the correlations obtained for both waves over different basins. The results show a stronger correlation between the region of maximum TD-like activity and high values of meridional gradients of moisture background instead of moisture background. The maximum differences in correlations are observed over the Atlantic region and the Indian Ocean with correlations (Table A1) as expected from Figs. 1 and 3. The same occurs for the equatorial Rossby waves.

REFERENCES

Adames, Á. F., 2017: Precipitation budget of the Madden–Julian oscillation. *J. Atmos. Sci.*, **74**, 1799–1817, https://doi.org/10.1175/JAS-D-16-0242.1.

——, 2021: Interactions between water vapor, potential vorticity and vertical wind shear in quasi-geostrophic motions: Implications for rotational tropical motion systems. *J. Atmos. Sci.*, **78**, 903–923, https://doi.org/10.1175/JAS-D-20-0205.1.

——, 2022: The basic equations under weak temperature gradient balance: Formulation, scaling, and types of convectively coupled motions. *J. Atmos. Sci.*, **79**, 2087–2108, https://doi.org/10.1175/JAS-D-21-0215.1.

——, and D. Kim, 2016: The MJO as a dispersive, convectively coupled moisture wave: Theory and observations. *J. Atmos. Sci.*, **73**, 913–941, https://doi.org/10.1175/JAS-D-15-0170.1.

——, and Y. Ming, 2018a: Interactions between water vapor and potential vorticity in synoptic-scale monsoonal disturbances: Moisture vortex instability. *J. Atmos. Sci.*, **75**, 2083–2106, https://doi.org/10.1175/JAS-D-17-0310.1.

——, and ——, 2018b: Moisture and moist static energy budgets of South Asian monsoon low pressure systems in GFDL AM4.0. *J. Atmos. Sci.*, **75**, 2107–2123, https://doi.org/10.1175/JAS-D-17-0309.1.

——, J. Patoux, and R. C. Foster, 2014: The contribution of extratropical waves to the MJO wind field. *J. Atmos. Sci.*, **71**, 155–176, https://doi.org/10.1175/JAS-D-13-084.1.

——, D. Kim, S. K. Clark, Y. Ming, and K. Inoue, 2019: Scale analysis of moist thermodynamics in a simple model and the relationship between moisture modes and gravity waves. *J. Atmos. Sci.*, **76**, 3863–3881, https://doi.org/10.1175/JAS-D-19-0121.1.

Adames-Corraliza, Á. F., and V. C. Mayta, 2024: The stirring tropics: Theory of moisture mode–Hadley cell interactions. *J. Climate*, **37**, 1383–1401, https://doi.org/10.1175/JCLI-D-23-0147.1.

Ahmed, F., 2021: The MJO on the equatorial beta plane: An eastward-propagating Rossby wave induced by meridional moisture advection. *J. Atmos. Sci.*, **78**, 3115–3135, https://doi.org/10.1175/JAS-D-21-0071.1.

——, J. D. Neelin, and Á. F. Adames, 2021: Quasi-equilibrium and weak temperature gradient balances in an equatorial beta-plane model. *J. Atmos. Sci.*, **78**, 209–227, https://doi.org/10.1175/JAS-D-20-0184.1.

Andersen, J. A., and Z. Kuang, 2012: Moist static energy budget of MJO-like disturbances in the atmosphere of a zonally symmetric aquaplanet. *J. Climate*, **25**, 2782–2804, https://doi.org/10.1175/JCLI-D-11-00168.1.

Arnold, N. P., M. Branson, Z. Kuang, D. A. Randall, and E. Tziperman, 2015: MJO intensification with warming in the superparameterized CESM. *J. Climate*, **28**, 2706–2724, https://doi.org/10.1175/JCLI-D-14-00494.1.

Betts, A. K., 1986: A new convective adjustment scheme. Part I: Observational and theoretical basis. *Quart. J. Roy. Meteor. Soc.*, **112**, 677–691, https://doi.org/10.1002/qj.49711247307.

——, and M. J. Miller, 1993: The Betts-Miller scheme. *The Representation of Cumulus Convection in Numerical Models*, *Meteor. Monogr.*, No. 24, Amer. Meteor. Soc., 107–121, https://doi.org/10.1007/978-1-935704-13-3_9.

Bretherton, C. S., M. E. Peters, and L. E. Back, 2004: Relationships between water vapor path and precipitation over the tropical oceans. *J. Climate*, **17**, 1517–1528, https://doi.org/10.1175/1520-0442(2004)017<1517:RBWVPA>2.0.CO;2.

Charney, J. G., 1963: A note on large-scale motions in the tropics. *J. Atmos. Sci.*, **20**, 607–609, https://doi.org/10.1175/1520-0469(1963)020<0607:ANOLSM>2.0.CO;2.

Chen, G., 2022: A model of the convectively coupled equatorial Rossby wave over the Indo-Pacific warm pool. *J. Atmos. Sci.*, **79**, 2267–2283, https://doi.org/10.1175/JAS-D-21-0326.1.

Dias, J., and G. N. Kiladis, 2014: Influence of the basic state zonal flow on convectively coupled equatorial waves. *Geophys. Res. Lett.*, **41**, 6904–6913, https://doi.org/10.1002/2014GL061476.

Diaz, M., and W. R. Boos, 2021: Evolution of idealized vortices in monsoon-like shears: Application to monsoon depressions. *J. Atmos. Sci.*, **78**, 1207–1225, https://doi.org/10.1175/JAS-D-20-0286.1.

Feng, T., X.-Q. Yang, J.-Y. Yu, and R. Huang, 2020: Convective coupling in tropical-depression-type waves. Part I: Rainfall characteristics and moisture structure. *J. Atmos. Sci.*, **77**, 3407–3422, https://doi.org/10.1175/JAS-D-19-0172.1.

Gill, A. E., 1980: Some simple solutions for heat-induced tropical circulation. *Quart. J. Roy. Meteor. Soc.*, **106**, 447–462, https://doi.org/10.1002/qj.49710644905.

Gonzalez, A. O., and X. Jiang, 2019: Distinct propagation characteristics of intraseasonal variability over the tropical west Pacific. *J. Geophys. Res. Atmos.*, **124**, 5332–5351, https://doi.org/10.1029/2018JD029884.

Hayashi, Y., 1973: A method of analyzing transient waves by space-time cross spectra. *J. Appl. Meteor.*, **12**, 404–408, https://doi.org/10.1175/1520-0450(1973)012<0404:AMOATW>2.0.CO;2.

——, 1977: On the coherence between progressive and retrogressive waves and a partition of space-time power spectra into standing and traveling parts. *J. Appl. Meteor.*, **16**, 368–373, https://doi.org/10.1175/1520-0450(1977)016<0368:OTCBPA>2.0.CO;2.

Hersbach, H., and Coauthors, 2019: Global reanalysis: Goodbye Era-Interim, hello ERA5. *ECMWF Newsletter*, No. 159, ECMWF, Reading, United Kingdom, 17–24, https://doi.org/10.21957/vf291hehd7.

Hodges, K. I., D. W. Chappell, G. J. Robinson, and G. Yang, 2000: An improved algorithm for generating global window brightness temperatures from multiple satellite infrared imagery. *J. Atmos. Oceanic Technol.*, **17**, 1296–1312, https://doi.org/10.1175/1520-0426(2000)017<1296:AIAFGG>2.0.CO;2.

Huaman, L., E. D. Maloney, C. Schumacher, and G. N. Kiladis, 2021: Easterly waves in the east Pacific during the OTREC 2019 field campaign. *J. Atmos. Sci.*, **78**, 4071–4088, https://doi.org/10.1175/JAS-D-21-0128.1.

Hunt, K. M. R., A. G. Turner, P. M. Inness, D. E. Parker, and R. C. Levine, 2016: On the structure and dynamics of Indian monsoon depressions. *Mon. Wea. Rev.*, **144**, 3391–3416, https://doi.org/10.1175/MWR-D-15-0138.1.

Inoue, K., Á. F. Adames, and K. Yasunaga, 2020: Vertical velocity profiles in convectively coupled equatorial waves and MJO: New diagnoses of vertical velocity profiles in the wavenumber-frequency domain. *J. Atmos. Sci.*, **77**, 2139–2162, https://doi.org/10.1175/JAS-D-19-0209.1.

Jiang, X., M. Zhao, E. D. Maloney, and D. E. Waliser, 2016: Convective moisture adjustment time scale as a key factor in regulating model amplitude of the Madden-Julian Oscillation. *Geophys. Res. Lett.*, **43**, 10 412–10 419, https://doi.org/10.1002/2016GL070898.

——, Á. F. Adames, M. Zhao, D. Waliser, and E. Maloney, 2018: A unified moisture mode framework for seasonality of the Madden–Julian oscillation. *J. Climate*, **31**, 4215–4224, https://doi.org/10.1175/JCLI-D-17-0671.1.

Kiladis, G. N., C. D. Thorncroft, and N. M. J. Hall, 2006: Three-dimensional structure and dynamics of African easterly waves. Part I: Observations. *J. Atmos. Sci.*, **63**, 2212–2230, https://doi.org/10.1175/JAS3741.1.

——, M. C. Wheeler, P. T. Haertel, K. H. Straub, and P. E. Roundy, 2009: Convectively coupled equatorial waves. *Rev. Geophys.*, **47**, RG2003, https://doi.org/10.1029/2008RG000266.

——, J. Dias, and M. Gehne, 2016: The relationship between equatorial mixed Rossby–gravity and eastward inertio-gravity waves. Part I. *J. Atmos. Sci.*, **73**, 2123–2145, https://doi.org/10.1175/JAS-D-15-0230.1.

Lau, K.-H., and N.-C. Lau, 1990: Observed structure and propagation characteristics of tropical summertime synoptic scale disturbances. *Mon. Wea. Rev.*, **118**, 1888–1913, https://doi.org/10.1175/1520-0493(1990)118<1888:OSAPCO>2.0.CO;2.

Livezey, R. E., and W. Y. Chen, 1983: Statistical field significance and its determination by Monte Carlo techniques. *Mon. Wea. Rev.*, **111**, 46–59, https://doi.org/10.1175/1520-0493(1983)111<0046:SFSAID>2.0.CO;2.

Madden, R. A., and P. R. Julian, 1972: Description of global-scale circulation cells in the tropics with a 40–50 day period. *J. Atmos. Sci.*, **29**, 1109–1123, https://doi.org/10.1175/1520-0469(1972)029<1109:DOGSCC>2.0.CO;2.

Matsuno, T., 1966: Quasi-geostrophic motions in the equatorial area. *J. Meteor. Soc. Japan*, **44**, 25–43, https://doi.org/10.2151/jmsj1965.44.1_25.

Mayta, V. C., and Á. F. Adames, 2021: Two-day westward-propagating inertio-gravity waves during GoAmazon. *J. Atmos. Sci.*, **78**, 3727–3743, https://doi.org/10.1175/JAS-D-20-0358.1.

——, and ——, 2023: Moist thermodynamics of convectively coupled waves over the Western Hemisphere. *J. Climate*, **36**, 2765–2780, https://doi.org/10.1175/JCLI-D-22-0435.1.

——, G. N. Kiladis, J. Dias, P. L. S. Dias, and M. Gehne, 2021: Convectively coupled Kelvin waves over tropical South America. *J. Climate*, **34**, 6531–6547, https://doi.org/10.1175/JCLI-D-20-0662.1.

——, Á. F. Adames, and F. Ahmed, 2022: Westward-propagating moisture mode over the tropical Western Hemisphere. *Geophys. Res. Lett.*, **49**, e2022GL097799, https://doi.org/10.1029/2022GL097799.

Núñez Ocasio, K. M., and R. Rios-Berrios, 2023: African easterly wave evolution and tropical cyclogenesis in a Pre-Helene (2006) hindcast using the Model for Prediction Across Scales-Atmosphere (MPAS-A). *J. Adv. Model. Earth Syst.*, **15**, e2022MS003181, https://doi.org/10.1029/2022MS003181.

Raymond, D. J., and Ž. Fuchs, 2009: Moisture modes and the Madden–Julian oscillation. *J. Climate*, **22**, 3031–3046, https://doi.org/10.1175/2008JCLI2739.1.

——, S. L. Sessions, A. H. Sobel, and Ž. Fuchs, 2009: The mechanics of gross moist stability. *J. Adv. Model. Earth Syst.*, **1** (9), https://doi.org/10.3894/JAMES.2009.1.9.

Rios-Berrios, R., B. Medeiros, and G. H. Bryan, 2020: Mean climate and tropical rainfall variability in aquaplanet simulations using the Model for Prediction across Scales–Atmosphere. *J. Adv. Model. Earth Syst.*, **12**, e2020MS002102, https://doi.org/10.1029/2020MS002102.

——, F. Judt, G. Bryan, B. Medeiros, and W. Wang, 2023: Three-dimensional structure of convectively coupled equatorial waves in aquaplanet experiments with resolved or parameterized convection. *J. Climate*, **36**, 2895–2915, https://doi.org/10.1175/JCLI-D-22-0422.1.

Russell, J. O. H., A. Aiyyer, and J. D. White, 2020: African easterly wave dynamics in convection-permitting simulations: Rotational stratiform instability as a conceptual model. *J. Adv. Model. Earth Syst.*, **12**, e2019MS001706, https://doi.org/10.1029/2019MS001706.

Rydbeck, A. V., and E. D. Maloney, 2014: Energetics of east Pacific easterly waves during intraseasonal events. *J. Climate*, **27**, 7603–7621, https://doi.org/10.1175/JCLI-D-14-00211.1.

——, and ——, 2015: On the convective coupling and moisture organization of east Pacific easterly waves. *J. Atmos. Sci.*, **72**, 3850–3870, https://doi.org/10.1175/JAS-D-15-0056.1.

Serra, Y. L., G. N. Kiladis, and M. F. Cronin, 2008: Horizontal and vertical structure of easterly waves in the Pacific ITCZ. *J. Atmos. Sci.*, **65**, 1266–1284, https://doi.org/10.1175/2007JAS2341.1.

——, ——, and K. I. Hodges, 2010: Tracking and mean structure of easterly waves over the intra-Americas Sea. *J. Climate*, **23**, 4823–4840, https://doi.org/10.1175/2010JCLI3223.1.

Snide, C. E., Á. F. Adames, S. W. Powell, and V. C. Mayta, 2022: The role of large-scale moistening by adiabatic lifting in the Madden–Julian oscillation convective onset. *J. Climate*, **35**, 269–284, https://doi.org/10.1175/JCLI-D-21-0322.1.

Sobel, A. H., and C. S. Bretherton, 2000: Modeling tropical precipitation in a single column. *J. Climate*, **13**, 4378–4392, https://doi.org/10.1175/1520-0442(2000)013<4378:MTPIAS>2.0.CO;2.

——, and T. Horinouchi, 2000: On the dynamics of easterly waves, monsoon depressions, and tropical depression type disturbances. *J. Meteor. Soc. Japan*, **78**, 167–173, https://doi.org/10.2151/jmsj1965.78.2_167.

——, and C. S. Bretherton, 2003: Large-scale waves interacting with deep convection in idealized mesoscale model simulations. *Tellus*, **55A**, 45–60, https://doi.org/10.3402/tellusa.v55i1.12084.

——, and E. Maloney, 2012: An idealized semi-empirical framework for modeling the Madden–Julian oscillation. *J. Atmos. Sci.*, **69**, 1691–1705, https://doi.org/10.1175/JAS-D-11-0118.1.

——, J. Nilsson, and L. M. Polvani, 2001: The weak temperature gradient approximation and balanced tropical moisture waves. *J. Atmos. Sci.*, **58**, 3650–3665, https://doi.org/10.1175/1520-0469(2001)058<3650:TWTGAA>2.0.CO;2.

Stoll, P. J., R. G. Graversen, and G. Messori, 2023: The global atmospheric energy transport analysed by a wavelength-based scale separation. *Wea Climate Dyn.*, **4** (1), 1–17, https://doi.org/10.5194/wcd-4-1-2023.

Takayabu, Y. N., 1994: Large-scale cloud disturbances associated with equatorial waves. Part I: Spectral features of the cloud disturbances. *J. Meteor. Soc. Japan*, **72**, 433–449, https://doi.org/10.2151/jmsj1965.72.3_433.

Trenberth, K. E., and D. P. Stepaniak, 2003: Covariability of components of poleward atmospheric energy transports on seasonal and interannual timescales. *J. Climate*, **16**, 3691–3705, https://doi.org/10.1175/1520-0442(2003)016<3691:COCOPA>2.0.CO;2.

Tulich, S., and G. Kiladis, 2021: On the regionality of moist Kelvin waves and the MJO: The critical role of the background zonal flow. *J. Adv. Model. Earth Syst.*, **13**, e2021MS002528, https://doi.org/10.1029/2021MS002528.

Vargas Martes, R. M., Á. F. Adames-Corraliza, and V. C. Mayta, 2023: The role of water vapor and temperature in the thermodynamics of tropical northeast Pacific and African easterly waves. *J. Atmos. Sci.*, **80**, 2305–2322, https://doi.org/10.1175/JAS-D-22-0177.1.

Wheeler, M., and G. N. Kiladis, 1999: Convectively coupled equatorial waves: Analysis of clouds in the wavenumber–frequency domain. *J. Atmos. Sci.*, **56**, 374–399, https://doi.org/10.1175/1520-0469(1999)056<0374:CCEWAO>2.0.CO;2.

——, ——, and P. J. Webster, 2000: Large-scale dynamical fields associated with convectively coupled equatorial waves. *J. Atmos. Sci.*, **57**, 613–640, https://doi.org/10.1175/1520-0469(2000)057<0613:LSDFAW>2.0.CO;2.

Wolding, B., J. Dias, G. Kiladis, F. Ahmed, S. W. Powell, E. Maloney, and M. Branson, 2020a: Interactions between moisture and tropical convection. Part I: The coevolution of moisture and convection. *J. Atmos. Sci.*, **77**, 1783–1799, https://doi.org/10.1175/JAS-D-19-0225.1.

——, ——, ——, E. Maloney, and M. Branson, 2020b: Interactions between moisture and tropical convection. Part II: The convective coupling of equatorial waves. *J. Atmos. Sci.*, **77**, 1801–1819, https://doi.org/10.1175/JAS-D-19-0226.1.

Yanai, M., S. Esbensen, and J.-H. Chu, 1973: Determination of bulk properties of tropical cloud clusters from large-scale heat and moisture budgets. *J. Atmos. Sci.*, **30**, 611–627, https://doi.org/10.1175/1520-0469(1973)030<0611:DOBPOT>2.0.CO;2.

Yasunaga, K., S. Yokoi, K. Inoue, and B. E. Mapes, 2019: Space–time spectral analysis of the moist static energy budget equation. *J. Climate*, **32**, 501–529, https://doi.org/10.1175/JCLI-D-18-0334.1.

Yu, J.-Y., and J. D. Neelin, 1994: Modes of tropical variability under convective adjustment and the Madden–Julian oscillation. Part II: Numerical results. *J. Atmos. Sci.*, **51**, 1895–1914, https://doi.org/10.1175/1520-0469(1994)051<1895:MOTVUC>2.0.CO;2.

Zhang, C., Á. F. Adames, B. Khouider, B. Wang, and D. Yang, 2020: Four theories of the Madden–Julian Oscillation. *Rev. Geophys.*, **58**, e2019RG000685, https://doi.org/10.1029/2019RG000685.